

# Enhanced Photoluminescence of Monolayer MoSe<sub>2</sub> in a Double Resonant Plasmonic Nanocavity with Fano Resonance and Mode Matching

Chenyang Li, Qifa Wang, Hang Diao, Zhen Hao, Weixing Yu, Kaihui Liu, Xuetao Gan,\*  
Fajun Xiao,\* and Jianlin Zhao\*

Two-dimensional transition metal dichalcogenides exhibit remarkable optical properties. However, their applications in electronics and photonics are severely limited by the intrinsically low absorption and emission rates. Here, the photoluminescence (PL) enhancement by integrating the monolayer MoSe<sub>2</sub> into an Ag nanowire-on-mirror (NWoM) nanocavity is reported. From the dark-field scattering spectrum, a Fano resonance resulting from the coupling between discrete exciton state of MoSe<sub>2</sub> and broad plasmon mode of nanocavity is observed. This Fano resonance, as a characteristic of intermediate plasmon–exciton coupling, shows remarkable ability to accelerate emission rate of MoSe<sub>2</sub>. Furthermore, the nanocavity with multiple resonances provides an excellent spatial mode overlap at excitation and emission wavelengths that affords the intriguing opportunity to resonantly enhance the absorption and PL quantum yield at the same location. The combination of Fano resonance and mode matching allows the attainment of over 1800-fold PL enhancement. These results provide a facile way to enhance the PL intensity of monolayer MoSe<sub>2</sub> that may facilitate highly efficient optoelectronic devices.

## 1. Introduction

Atomically thin transition metal dichalcogenides (TMDs) have attracted growing interest owing to their extraordinary optical properties. Unlike their bulk counterparts, monolayer TMDs such as MoS<sub>2</sub>, MoSe<sub>2</sub>, WS<sub>2</sub>, and WSe<sub>2</sub> exhibit a direct bandgap that allows more efficient photon absorption and emission via transitions at the fundamental gap.<sup>[1]</sup> Because of the reduced dielectric screening, TMDs show strong Coulomb interaction that leads to the formation of tightly bound electron-hole pairs (excitons).<sup>[2]</sup> In addition, the broken inversion symmetry and strong spin–orbit coupling in monolayer TMDs result in the fascinating valley- and spin-dependent optical and electrical properties.<sup>[3]</sup> These unique features hold a great promise for exploring novel optoelectronic applications such as photodetectors,<sup>[4]</sup> solar cells,<sup>[5]</sup> light-emitting devices, (LEDs)<sup>[6]</sup> and nanolasers.<sup>[7]</sup> However, inherited

from the atomically thin nature, the weak absorption and low photoluminescence (PL) quantum yield become fundamental obstacles to high-performance TMD-based devices.<sup>[8,9]</sup> A promising way to address this issue is the incorporation of the monolayer TMDs with plasmonic nanostructures.<sup>[10]</sup> Due to the strong local-field enhancement effect, plasmonic nanostructures show remarkable abilities to enhance the absorption of TMDs, meanwhile, to accelerate the spontaneous emission rate through the Purcell effect.<sup>[11]</sup> Until now, strong plasmon–exciton interactions with large PL enhancement have been demonstrated in a variety of designs, including patterned metallic arrays,<sup>[12]</sup> nanoantennas,<sup>[13]</sup> and colloidal nanoparticles.<sup>[14,15]</sup>

Particle-on-mirror (PoM) nanocavity, composed of the closely spaced metallic nanoparticle and ultrasmooth film, is an emerging plasmonic platform with the extremely small mode volume and remarkably strong field enhancement.<sup>[16]</sup> Different from the conventional plasmonic structures relying on top-down fabrication approaches, the PoM nanocavities, benefitting from the thin film deposition and bottom-up assembly techniques, possess the merits of subnanometer precision in gap-size control and readily tailored optical resonances. Therefore, they are highly favorable

C. Li, Q. Wang, H. Diao, Z. Hao, X. Gan, F. Xiao, J. Zhao  
Key Laboratory of Light Field Manipulation and Information Acquisition  
Ministry of Industry and Information Technology  
and Shaanxi Key Laboratory of Optical Information Technology  
School of Physical Science and Technology  
Northwestern Polytechnical University  
Xi'an 710129, China  
E-mail: xuetaogan@nwpu.edu.cn; fjxiao@nwpu.edu.cn;  
jlzhao@nwpu.edu.cn

W. Yu  
Key Laboratory of Spectral  
Imaging Technology of Chinese Academy of Sciences  
Xi'an Institute of Optics and Precision Mechanics of Cas  
Xi'an 710119, China

K. Liu  
State Key Laboratory for Mesoscopic Physics  
Collaborative Innovation Centre of Quantum Matter  
School of Physics  
Peking University  
Beijing 100871, China

The ORCID identification number(s) for the author(s) of this article can be found under <https://doi.org/10.1002/lpor.202100199>

DOI: 10.1002/lpor.202100199

for exploring the light-matter interactions at the nanoscale. Recently, impelled by the promising applications in future optoelectronics and nanophotonics devices, a wealth of PoM configurations, such as the metallic film-coupled nanosphere,<sup>[17]</sup> nanocube,<sup>[18,19]</sup> and nanowire,<sup>[20,21]</sup> have been successfully used to enhance the PL of TMDs. Since the resonant mode of plasmonic PoM nanocavity has a broad bandwidth, it can naturally match the spectrally broad spontaneous emission to accelerate the radiative rate of the material. Particularly, when the plasmon mode in the nanocavity moderately couples with the exciton<sup>[22]</sup> or even with higher-order excitonic quasiparticles of TMDs,<sup>[20,21]</sup> a Fano lineshape will appear in the scattering or the extinction spectrum of the hybrid system. In this case, the Fano resonance can boost the emission rate of the hybrid system utmost,<sup>[23]</sup> facilitating the implementation of high-efficiency TMD-based LED.<sup>[20,21]</sup> Also, by carefully molding the structure or selecting the mode type of nanocavity, the directionality of spontaneous emission can be aligned to be a specific spatial direction to achieve a high collection efficiency.<sup>[22,24]</sup> Moreover, plasmon resonances of the PoM nanocavity can be tuned by varying the gap size,<sup>[25]</sup> the thickness of dielectric coating layer,<sup>[26]</sup> and the size and shape of particle,<sup>[25]</sup> showing a large flexibility in tailoring the emission spectrum.

Generally, for enhanced spectroscopies, it is quite desirable to introduce multiple resonances in the system to enhance both the excitation and scattering (radiative) processes. This is valid for a host of nonlinear optical phenomena including two-photon absorption,<sup>[27]</sup> second harmonic generation,<sup>[28]</sup> and wave mixings.<sup>[29]</sup> Likewise, to obtain a giant PL intensity, the double resonance requirement is still indispensable. Until now, many studies of PL enhancement merely concentrate on accelerating the emission rate through the interaction between the single dipolar resonance of PoM nanocavity and the exciton of TMDs.<sup>[18,30–32]</sup> Notice that with the large particle size or control of morphology, the PoM nanocavity can also support multipolar accessible resonances.<sup>[23,33,34]</sup> These high order modes, possessing more intense near field, are highly desirable to boost the excitation rate of PL. However, it remains scarce to fully exploit the benefit of the double resonance to augment both excitation and emission processes.<sup>[19]</sup> Here, we demonstrate a hybrid system by inserting the monolayer MoSe<sub>2</sub> into a silver (Ag) nanowire-on-mirror (NWoM) nanocavity with multiple resonances. From the dark scattering spectrum, it reveals a Fano resonance resulting from the coherent interaction between the discrete exciton state of MoSe<sub>2</sub> and the broadband low-order plasmon mode. An 1840-fold enhancement in PL intensity of MoSe<sub>2</sub> is further observed by spectrally aligning the light absorption and exciton emission to the high-order plasmon mode and Fano resonance, meanwhile, ensuring a good spatial overlap between these two enhancement processes.

## 2. Results and Discussion

The geometry of the NWoM is schematically displayed in **Figure 1a**, where the atomically flat Au film and PVP coated Ag nanowire (NW) are successively separated by 1.5 nm thick Al<sub>2</sub>O<sub>3</sub> layer, the monolayer MoSe<sub>2</sub>, and 2 nm thick Al<sub>2</sub>O<sub>3</sub> layer. The Ag NW width is defined by its lateral length denoted as *d* in **Figure 1a**.

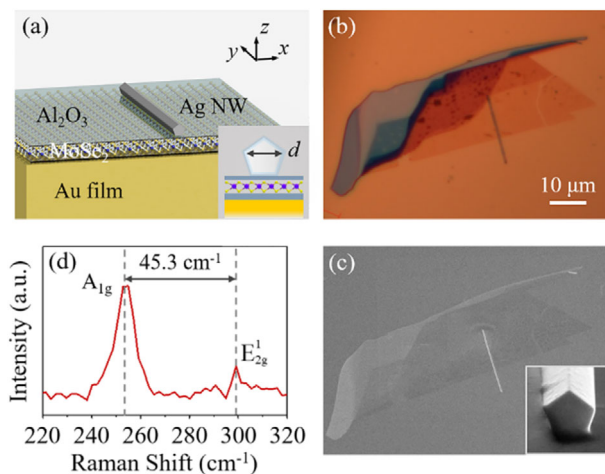


**Figure 1.** a) Schematic of Ag nanowire-on-mirror (NWoM) nanocavity encapsulating monolayer MoSe<sub>2</sub>. The inset of (a) shows the cross-section diagram of NWoM with the geometry parameter. b) Optical and c) SEM images of the NWoM. The inset of (c) shows the side view SEM image of Ag NW. d) Raman spectrum of the monolayer MoSe<sub>2</sub> taken nearby the NWoM.

This Ag NW with a length of 18.6 μm is partially overlapped with the MoSe<sub>2</sub> flake (see **Figure 1b,c**), in order to determine the interaction between the plasmon mode of NWoM and the exciton of MoSe<sub>2</sub>. As shown in the inset of **Figure 1c**, the Ag NW has a pentagonal cross-section with rounded corners and a crystal facet of Ag NW parallel with the underneath Au film, forming a metal-insulator-metal (MIM) vertical nanocavity. The monolayer region of MoSe<sub>2</sub> has a typical dimension of 11 × 40 μm<sup>2</sup>. Its monolayer nature is confirmed by Raman spectrum carried out on a commercial confocal microscope (WITec, Alpha 300R). As shown in **Figure 1d**, the out-of-plane mode A<sub>1g</sub> and the in-plane mode E<sub>2g</sub><sup>1</sup> have an interval of 45.3 cm<sup>-1</sup>, coinciding with the typical mode separation in the monolayer MoSe<sub>2</sub>.<sup>[35]</sup>

We first perform the scattering spectrum measurements on the individual NWoM nanocavity without the monolayer MoSe<sub>2</sub> in between via the dark-field micro-spectroscopy (see Experimental Section). As seen from **Figure 2a**, the scattering spectrum of NWoM with *d*=270 nm shows three pronounced resonances labeled as (1)–(3) whose peak positions can be acquired by decomposing the scattering spectrum with multiple Lorentzian functions (dashed lines in **Figure 2a**). These peaks are then well reproduced by the simulation based on the finite element method (FEM, see Experimental Section) as shown in **Figure 2b**. To unravel the origin of these resonances, we display the transient surface charge distributions of nanocavity modes (1)–(3) in the top panels of **Figure 2c–e**, respectively. From the charge maps, we attribute these modes to the plasmon hybridization between the vertical aligned quadrupole of NW and waveguide modes of MIM nanocavity (see **Figure S2**, Supporting Information).<sup>[36,37]</sup> The vertical quadrupole, featured with the neutral charge nodes locating at the vertex and bottom of NW, is excited due to the phase retardation effect and the considerable *z* component of p-polarized illumination (see **Figure S1**, Supporting Information). The waveguide modes can be interpreted

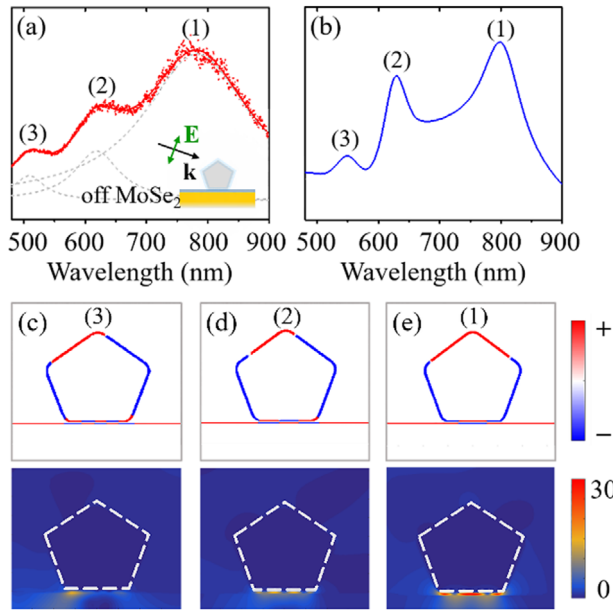


**Figure 2.** a) Experimental and b) simulated scattering spectra of NWoM nanocavity ( $d=270$  nm). The inset of (a) shows the illumination configuration. The scattering spectrum is decomposed into modes (1)–(3) with multiple Lorentzian functions (dashed lines). c–e) the charge (top panels) and electric field enhancement maps (bottom panels) of modes (1)–(3).

as Fabry–Perot resonances of the MIM nanocavity, that is, the standing waves of surface plasmon polaritons (SPPs) after the multi-reflections by the two edges of the NW bottom facet. Note that for each mode, opposite charges are present at the bottom facet of NW and Au film with the charge nodal points indicating the resonance order. The strong plasmon hybridization makes these nanocavity modes possess a large electric field enhancement within the gap region as shown in the bottom panels of Figure 2c–e. Especially, the mode (1) displays an over 30-fold of electric field enhancement factor, which is highly favorable to embed the monolayer MoSe<sub>2</sub> into the nanocavity to produce a strong plasmon–exciton interaction.

Figure 3a shows the scattering spectrum of NWoM ( $d=270$  nm) after the integration of a monolayer MoSe<sub>2</sub> in the gap. In comparison to that without MoSe<sub>2</sub>, two interesting features arise in the scattering spectrum: (i) due to the dielectric screening and dissipation channel provided by the monolayer MoSe<sub>2</sub>, the nanocavity modes get redshifted and broaden, resulting in the merging of modes (1) and (2); and (ii) an asymmetric lineshape featured with a dip appears in the spectral range of mode (1). As the spectral dip locates at the wavelength of neutral exciton ( $X^0$ ) of MoSe<sub>2</sub>, we ascribe this asymmetric spectral lineshape as a consequence of the Fano resonance, that is, a coupling between the neutral exciton of MoSe<sub>2</sub> and the plasmonic nanocavity mode (1). In the exciton–plasmon coupling system, the lifetime of exciton is much longer than that of plasmon. Therefore, it analogously provides two paths, that is, one towards the exciton related discrete state and the other towards the plasmon mode dominated continuous state. These two optical paths interfere destructively on the blue, and constructively on the red side of the Fano resonance, giving rise to the asymmetric spectral lineshape. To pro-

vide a deeper insight, we employ a coupled oscillators model to describe the Fano resonance.<sup>[38–40]</sup>

$$\begin{aligned} \ddot{X}_{\text{pl}} + \gamma_{\text{pl}}\dot{X}_{\text{pl}} + \omega_{\text{pl}}^2 X_{\text{pl}} + gX_{\text{A}} &= E_0 e^{i\omega t} \\ \ddot{X}_{\text{A}} + \gamma_{\text{A}}\dot{X}_{\text{A}} + \omega_{\text{A}}^2 X_{\text{A}} + gX_{\text{pl}} &= 0 \end{aligned} \quad (1)$$

where  $\omega_{\text{pl}}$ ,  $\omega_{\text{A}}$ , and  $\gamma_{\text{pl}}$ ,  $\gamma_{\text{A}}$  are the frequencies and damping rates of the uncoupled plasmon mode and exciton,  $g$  represents the coupling strength, and  $E_0 e^{i\omega t}$  denotes the external driving force of the system. According to Equation (1), the Fano lineshape in the scattering spectrum can be described as<sup>[40]</sup>

$$\sigma_{\text{sca}}(\omega) \propto \omega^4 \left| \frac{(\omega_{\text{A}}^2 - \omega^2 - i\gamma_{\text{A}}\omega)}{(\omega^2 - \omega_{\text{pl}}^2 + i\gamma_{\text{pl}}\omega)(\omega^2 - \omega_{\text{A}}^2 + i\gamma_{\text{A}}\omega) - \omega^2 g^2} \right|^2 \quad (2)$$

The theoretical fitting of scattering spectrum is shown as the solid line of Figure 3a, demonstrating a good agreement with the experiment result. Here, modes (2) and (3) are far from the exciton energy, which are therefore still reproduced by Lorentzian functions in the fitting.

We subsequently carry out the PL measurements of the hybrid system by using both 532 and 633 nm excitations, which have good spectral overlaps with modes (3) and (2), respectively. As can be seen from Figure 3b, with the same laser power (0.4 mW), 532 nm excitation achieves a higher PL enhancement in the NWoM region (green line in Figure 3b) as compared to that using 633 nm excitation (red line in Figure 3b). The reason lies in the monolayer MoSe<sub>2</sub> having a higher intrinsic absorption at 532 nm over that at 633 nm.<sup>[41]</sup> In addition, as seen from Figure 2c,d, the 532 nm excitation has a better performance in electric field enhancement in comparison to the 633 nm pump laser, leading to a higher excitation rate. As a result, the 532 nm excitation produces a nearly 100-fold enhancement in PL peak intensity relative to that taken from the MoSe<sub>2</sub> on the quartz substrate (black line in Figure 3b). Considering that the enhanced PL spectrum is contributed from both the region of NWoM and the background MoSe<sub>2</sub>, while, the truly active area for boosting the PL intensity is beneath the NW as shown in Figure 2c–e. To extract the real PL enhancement resulting from the NWoM, we define the PL enhancement factor as:

$$EF = \frac{I_{\text{NW}} - I_0}{I_0} \frac{S_0}{S_{\text{NW}}} \quad (3)$$

where  $I_{\text{NW}}$  and  $I_0$  are the PL intensities from the MoSe<sub>2</sub> area containing the NWoM nanocavity and on the quartz substrate, respectively.  $S_0$  denotes the excitation area of the laser spot size ( $\sim 16.0 \mu\text{m}^2$ ), and  $S_{\text{NW}}$  represents the area of NWoM within the laser spot ( $\sim 1.2 \mu\text{m}^2$ ). After correcting by Equation (3), the PL enhancement factor is found to be 1393 for the 532 nm excitation. Such large PL enhancement is ascribed to the plasmon-enhanced excitation and emission processes, which are further understood based on full wave simulations of the nanocavity (see Experimental Section). The excitation rate in free space is governed by the interaction of the incident electric field  $\mathbf{E}_0$  and the transition dipole of exciton  $\mathbf{p}$ , following  $\gamma_{\text{ex}}^0 \propto |\mathbf{p} \cdot \mathbf{E}_0|^2$ .<sup>[42]</sup> The enhanced excitation can be regarded as the relevant excitation rate between the NWoM-coupled and -uncoupled monolayer MoSe<sub>2</sub>

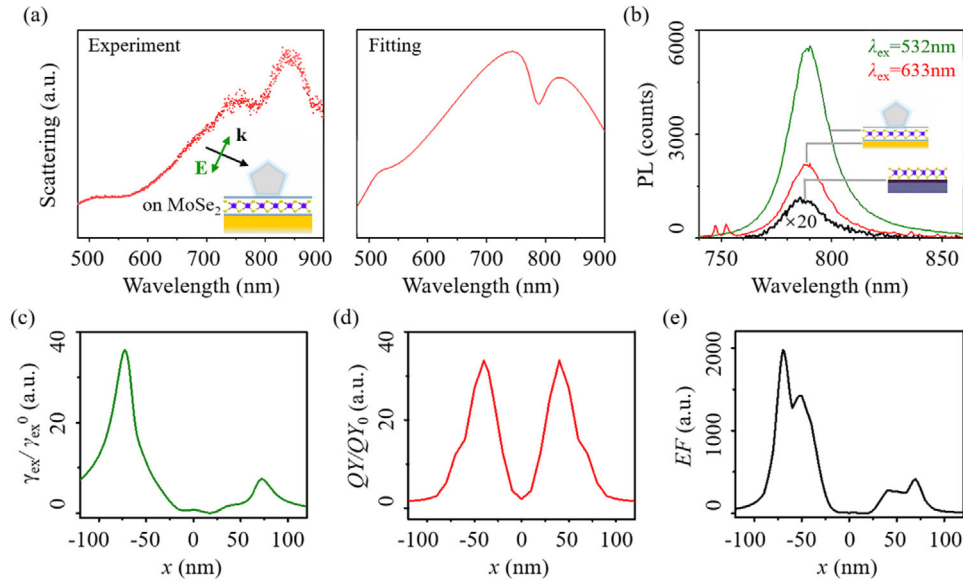


**Figure 3.** a) Measured (dots) and coupled oscillators model (COM) fitted scattering spectra (solid lines) of NWoM nanocavity ( $d=270$  nm) coupled with monolayer MoSe<sub>2</sub>. The inset of (a) shows the illumination configuration. b) Photoluminescence (PL) spectra from monolayer MoSe<sub>2</sub> on the SiO<sub>2</sub>/Si substrate (black line) and embedded in the NWoM nanocavity. The green and red lines are for the excitations of 532 and 633 nm, respectively. c) Spatial map of the excitation rate enhancement  $\gamma_{ex}/\gamma_{ex}^0$  relative to free space at the wavelength of 532 nm. d) Distribution of quantum-yield enhancement  $QY/QY_0$  at the wavelength of 789 nm. e) Calculated PL enhancement factor  $EF$ .

$\gamma_{ex}/\gamma_{ex}^0$ . Aware that the PL of monolayer MoSe<sub>2</sub> is dominated by the in-plane transition dipole,<sup>[43–45]</sup> Figure 3c displays the relevant excitation rate at the wavelength of 532 nm by adopting the enhancement of in-plane electric field intensity  $|E_{||}|^2/|E_{||}^0|^2$  as  $\gamma_{ex}/\gamma_{ex}^0$ . The considerable enhancement of excitation rate is observed at the edge of the NW bottom facet, with a maximum factor of 36-fold. On the other hand, the emission peak of PL locates around the Fano dip that makes the hybrid system acquire a large light-emitting capacity to boost the quantum yield of MoSe<sub>2</sub>. We assume that  $\gamma_r$  and  $\gamma_{nr}$  are the radiation and non-radiation exciton decay rates in the presence of nanocavity, and the intrinsic nonradiation decay rate  $\gamma_{int}^0$  remains unchanged. Then, the quantum yield of MoSe<sub>2</sub> embedded in the nanocavity is given by  $QY=\gamma_r/(\gamma_r+\gamma_{nr}+\gamma_{int}^0)$ . By employing the dyadic Green's function (see Experimental Section), we calculate the enhanced quantum yield as shown in Figure 3d. Of note is that the enhanced quantum yield exhibits an excellent spatial overlap with the enhanced excitation rate. This spatial overlap works with the multi-resonances merit of the nanocavity to allow the excitation and emission rates of MoSe<sub>2</sub> to be simultaneously boosted at the same location, rendering a significant enhanced PL intensity. Accordingly, the PL enhancement factor relative to MoSe<sub>2</sub> on quartz substrate can be stated as a product of the excitation and quantum yield enhancement,<sup>[19]</sup>

$$EF(\mathbf{r}, \omega_{ex}, \omega_{em}) = \frac{\eta}{\eta_0} \frac{\gamma_{ex}(\mathbf{r}, \omega_{ex})}{\gamma_{ex}^0(\mathbf{r}, \omega_{ex})} \frac{QY(\mathbf{r}, \omega_{em})}{QY_0(\mathbf{r}, \omega_{em})} \quad (4)$$

where  $\eta=65\%$  and  $\eta_0=14\%$  are the PL collection efficiencies for samples with the nanocavity and on the quartz substrate.  $\omega_{ex}$  and  $\omega_{em}$  are, respectively, for the excitation and emission frequencies. Figure 3e shows the distribution of PL enhancement factor cal-

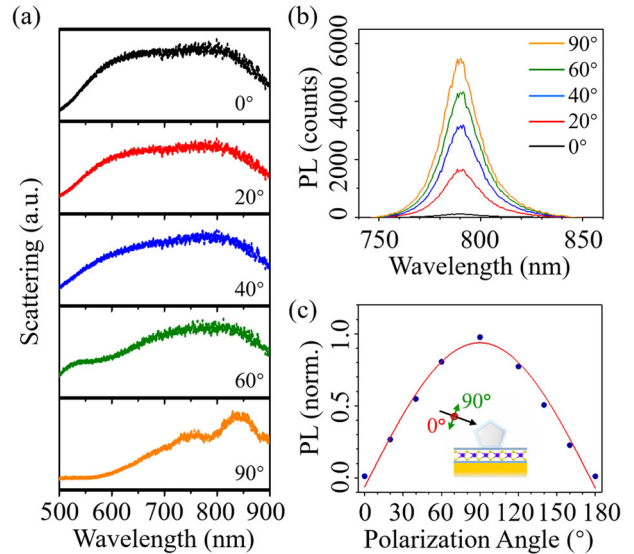


**Figure 4.** a) Scattering spectra of NWoM nanocavity ( $d=270$  nm) coupled with monolayer MoSe<sub>2</sub> under different polarization angles. b) PL spectra of monolayer MoSe<sub>2</sub> embedded in NWoM nanocavity under different polarization angles. c) Polarization-dependence of the PL peak intensity. 90° and 0° represents the polarization perpendicular and parallel to the nanowire axis, respectively.

culated from Equation (4), which exhibits the maximum value (1970) at the bottom edge of NW as expected.

To further elucidate the mechanism of PL enhancement, we perform the polarization dependent measurements on the MoSe<sub>2</sub> integrated NWoM ( $d=270$  nm). Figure 4a presents the polarization-resolved scattering spectra of the hybrid system. It

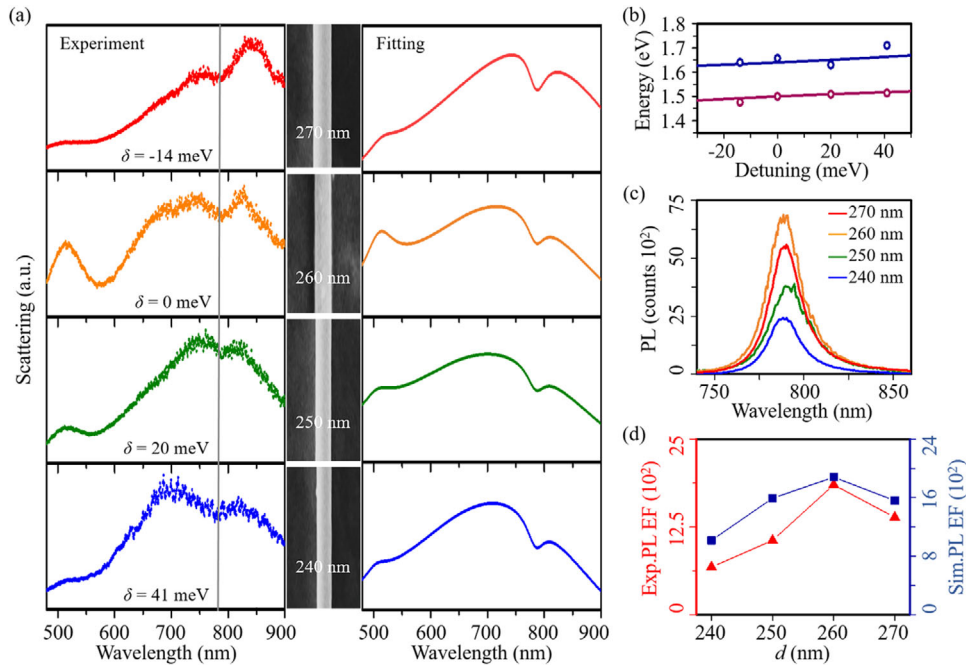


**Figure 5.** a) Scattering (dots) and COM fitted spectra (solid lines) of NWoM coupled with monolayer MoSe<sub>2</sub> for the NW width varied from 270 to 240 nm. The middle panels of (a) show the SEM images of NWs. b) Two scattering peaks of Fano lineshape against detuning. Blue and purple dots indicate experimental data extracted from scattering spectra. The solid lines are fitting results from the coupled oscillators model. c) Enhanced PL spectra of monolayer MoSe<sub>2</sub> for different NW widths. d) Measured (red dots) and calculated (blue dots) PL enhancement factor *EF* versus the NW width.

is found that the scattering spectrum rapidly loses the Fano line-shape and eventually evolves into a barely flat plateau as the excitation is changed from p-polarization (90°) to s-polarization (0°). This indicates the nanocavity modes (1)–(3) inherit the SPP character from the MIM waveguide modes, which exclusively exist for TM polarization (p-polarized component). With decreasing of the polarization angle, the attenuation in the p-polarized component successively takes the merits of the Fano resonance (60°), high order resonance (40°), and low order resonance (0°) away from the hybrid system. Consequently, the peak intensity of PL has an obvious decline accompanied with the decrease of the polarization angle (see Figure 4b), confirming the large PL enhancement in Figure 3b is attributed to the cooperation of the Fano resonance and the higher order nanocavity mode. The PL peak intensity as a function of polarization angle is summarized in Figure 4c, which is highly anisotropic and can be fitted to a sine curve with the maximum (minimum) PL intensity at the polarization angle of 90° (0° or 180°).

To realize an optimized plasmon–exciton coupling, the nanocavity mode (1) is further tuned across the frequency of MoSe<sub>2</sub> neutral exciton by decreasing the width of NW. Here, the thickness of dielectric spacer is kept as a constant. A blue shift of mode (1) from 785 to 770 nm is observed in the spectra of NWoMs without the embedded MoSe<sub>2</sub> when the width of NW is varied from 270 to 240 nm (see Figure S5a, Supporting Information). Considering the hybrid system will result in the redshift of plasmon mode (~10 nm), this tuning range of mode (1) well covers the neutral exciton of MoSe<sub>2</sub> (789 nm) to ensure the observation of different detuning states ( $\delta = \omega_{\text{pl}} - \omega_{\text{A}}$ ) of the plasmon–exciton coupling. The scattering spectra of the hybrid

system with different detunings are displayed in the left column of Figure 5a. As seen, the position of Fano dip remains unchanged against the detuning, corresponding to the wavelength of the neutral exciton (highlighted by a gray line). For a negative detuning, Fano dip splits a shoulder peak at the short wavelength part of mode (1). When the detuning is increased to be positive, this shoulder peak gradually becomes dominated. More interestingly, it is found that the mode (1) is splitted into two even peaks with zero detuning. These experimental scattering spectra are further fitted to the coupled oscillators model as shown in the right column of Figure 5a. It is revealed from the fitting that the coupling strength ( $g = 70$  meV) at zero detuning is larger than the exciton damping rate ( $\gamma_{\text{A}} = 43$  meV) but smaller than the plasmon damping rate ( $\gamma_{\text{pl}} = 250$  meV), indicating the hybrid system enters an intermediate coupling regime.<sup>[13,40]</sup> After removing the contributions of modes (2) and (3) from the scattering spectra (see Figure S5b, Supporting Information), we show the dependence of two scattering peaks beside the Fano dip on the detuning in Figure 5b. An anti-crossing behavior that can be described by  $E_{\pm} = (E_{\text{A}} + E_{\text{pl}})/2 \pm \sqrt{g^2 + \delta^2}/4$  (solid line in Figure 5b) is found,<sup>[13]</sup> where  $E_{\text{A}}$  and  $E_{\text{pl}}$  are the energies of neutral exciton and plasmon mode, respectively. In Figure 5c, we examine the enhanced PL spectra excited by 532 nm laser for the hybrid system with different detunings. As clearly seen from the Figure 5d (red dots), the enhanced PL peak intensity strongly depends on the detuning with a maximum enhancement factor (1840-fold) achieved at zero detuning ( $d = 260$  nm). The theoretical calculation of PL enhancement factor is presented as blue dots in Figure 5d, which quantitatively agrees well with the experimental results.

### 3. Conclusion

In summary, we have developed an approach to enhance the PL emission by integrating the monolayer MoSe<sub>2</sub> into an Ag NWoM nanocavity with multi-resonances. It is found that the plasmon–exciton coupling of the hybrid system results in a Fano resonance evidenced by an asymmetric lineshape in the scattering spectrum. A further delicate tuning of the Fano resonance reveals the hybrid system accesses to the intermediate coupling regime. Such intermediate coupling allows us to take full advantages of the plasmonic confinement and the strong excitonic effect to boost the PL radiative rate utmost. Moreover, the multi-resonances feature of the nanocavity ensures not only a simultaneous enhancement of absorption and emission processes, but also an excellent spatial overlap between these two enhanced processes, giving rising to an 1840-fold PL enhancement. This work provides a flexible and tunable platform to manipulate the plasmon–exciton coupling and benefits the implementations of future optoelectronic devices including the nanoscale light sources, photodetectors, and photovoltaics.

### 4. Experimental Section

**Sample Fabrication:** First, a 50 nm thick Au film was deposited on a silicon wafer by thermal evaporation at a deposition rate of 1 Ås<sup>-1</sup>, which was transferred onto a SiO<sub>2</sub>/Si substrate via a template-stripping method to form an ultrasmooth interface with the back side of Au film (~0.3 nm in roughness). Subsequently, to prevent fluorescence quenching, an Al<sub>2</sub>O<sub>3</sub> spacer layer (~1.5 nm of thickness) was deposited on the ultrasmooth gold film using atomic layer deposition (ALD) at the temperature of 90 °C. Afterward, the monolayer MoSe<sub>2</sub> was mechanically exfoliated from bulk crystal (hq-graphene, Inc.), then was deterministically transferred onto the Al<sub>2</sub>O<sub>3</sub> layer with the help of a polydimethylsiloxane gel-film. To protect the MoSe<sub>2</sub> flake, a 2 nm thick Al<sub>2</sub>O<sub>3</sub> layer was then deposited on the MoSe<sub>2</sub>–Au hybrid structure using ALD. Next, the Ag NW wrapped by 3 nm PVP layer (XFNANO, Co., Ltd) was drop-cast on the Al<sub>2</sub>O<sub>3</sub> layer coated Au film to form the NWoM. Finally, to integrate the MoSe<sub>2</sub> in the nanocavity, a three-axis commercial micromanipulator equipped with tungsten probes was used to precisely move the Ag NW to overlay on the monolayer MoSe<sub>2</sub>.

**Optical Characterization:** The scattering spectra of the NWoMs were characterized using a home-built dark-field micro-spectroscopy system (see Figure S7, Supporting Information), where a polarization-controlled white light from a halogen lamp was obliquely illuminated on the sample through a 50× objective (Mitutoyo, NA 0.55) at an incident angle of 70°. The scattering light was collected with an upright 50× objective (Nikon NA 0.4), then was recorded by a CCD camera as the dark-field image. Meanwhile, the light scattered from the NWoMs was imaged through a pinhole aperture onto a CCD-equipped spectrometer (Andor Shamrock SR-3031-B) for the spectral analysis. The PL measurements were carried out on the same micro-spectroscopy system. The collimated 532 and 633 nm pump lasers were kept at a power of ~0.4 mW and were focused on the sample through the side-illuminating objective, producing a ~30 μm<sup>2</sup>-sized spot at the focal plane. The backscattered PL emission was collected by the same upright objective and the collection area was selected and controlled to be ~16 μm<sup>2</sup> by adjusting the position and size of pinhole. After passing through a long-pass filter, the collected emission was delivered to the spectrometer to obtain the PL spectrum.

**Numerical Simulation:** Full-wave electromagnetic simulations were performed with the finite element method (FEM). In the simulations, a 2D model was adopted considering the length of Ag NW is much larger than the transverse dimension of NWoMs. The geometry parameters of the nanocavity were taken as their experimental counterparts. The permittivity of Au and Ag were taken from the experimental data of Johnson and Christy.<sup>[46]</sup> The refractive indices of the PVP and Al<sub>2</sub>O<sub>3</sub> layer were set to be

1.5. For the scattering calculations, the authors used a plane wave with an incident angle of 70° as the excitation. The scattering field was obtained by a two-step method, where the background electric field was first calculated in the absence of Ag NW and then was used to arrive at the total field with the present of Ag NW. The scattered field at each wavelength was collected within a solid angle of 47° corresponding to NA=0.4 to acquire the scattering spectrum. The surface charge density was derived by calculating the difference of the normal component of the electric field with respect to the metal surface.

The quantum yield enhancement was calculated with the finite-difference time-domain method (FDTD), where the monolayer MoSe<sub>2</sub> was set as a monochromatic point dipole ( $\lambda_{em}=789$  nm) with a horizontal orientation. This emission dipole was placed in the nanocavity as modeled in the scattering simulation. The Green's function of the hybrid system was computed by varying the position of the dipole emitter on a discrete grid (1 × 25) beneath the Ag NW.<sup>[42]</sup> According to the Green's function, the ratio of the radiative decay rate ( $\gamma_{rad}$ ) and the total decay rate ( $\gamma_{sp}=\gamma_{rad}+\gamma_{loss}$ ) to the intrinsic radiative decay rate ( $\gamma_{rad}^0$ ) were obtained by the transmission box enclosing the entire domain and the dipole emitter, respectively. Then, the radiative QY was then given by

$$QY = \frac{\gamma_{rad}/\gamma_{rad}^0}{\gamma_{rad}/\gamma_{rad}^0 + \gamma_{loss}/\gamma_{rad}^0 + (1 - Q_0)/Q_0} \quad (5)$$

where  $Q_0=5\%$  is the intrinsic quantum yield of the monolayer of MoSe<sub>2</sub>.<sup>[47]</sup>

### Supporting Information

Supporting Information is available from the Wiley Online Library or from the author.

### Acknowledgements

The authors are thankful for the support by the National key R&D Program of China (2017YFA0303800), the National Natural Science Foundation of China (NSFC) (11634010, 11874050, 91950119, 61905196), Shaanxi Provincial Key R&D Program (2021KW-19), the Pearl River Talent Recruitment Program of Guangdong Province (2019ZT08C321), Fundamental Research Funds for the Central Universities (3102019JC008, D5000210936), Open Research Fund of CAS Key Laboratory of Spectral Imaging Technology (No. LSIT201913W), and the SEM measurements by the Analytical and Testing Center of Northwestern Polytechnical University.

### Conflict of Interest

The authors declare no conflict of interest.

### Data Availability Statement

The data that support the findings of this study are available from the corresponding author upon reasonable request.

### Keywords

Fano resonance, monolayer MoSe<sub>2</sub>, photoluminescence enhancement, plasmonic nanocavities, Purcell effect

Received: April 13, 2021  
Revised: September 23, 2021  
Published online:

- [1] F. Xia, H. Wang, D. Xiao, M. Dubey, A. Ramasubramaniam, *Nat. Photonics* **2014**, *8*, 899.
- [2] T. Mueller, E. Malic, *NPJ 2D Mater. Appl.* **2018**, *2*, 29.
- [3] K. F. Mak, J. Shan, *Nat. Photonics* **2016**, *10*, 216.
- [4] O. Lopez-Sanchez, D. Lembke, M. Kayci, A. Radenovic, A. Kis, *Nat. Nanotechnol.* **2013**, *8*, 497.
- [5] D. Q. Zheng, Z. Zhao, R. Huang, J. Nie, L. Li, Y. Zhang, *Nano Energy* **2017**, *32*, 448.
- [6] D. Andrzejewski, R. Oliver, Y. Beckmann, A. Grundmann, M. Heuken, H. Kalisch, A. Vescan, T. Kümmell, G. Bacher, *Adv. Opt. Mater.* **2020**, *8*, 2000694.
- [7] Y. Ye, Z. J. Wong, X. Lu, X. Ni, H. Zhu, X. Chen, Y. Wang, X. Zhang, *Nat. Photonics* **2015**, *9*, 733.
- [8] K. F. Mak, K. He, C. Lee, G. H. Lee, J. Hone, T. F. Heinz, J. Shan, *Nat. Mater.* **2013**, *12*, 207.
- [9] K. F. Mak, C. Lee, J. Hone, J. Shan, T. F. Heinz, *Phys. Rev. Lett.* **2010**, *105*, 136805.
- [10] X. Li, J. Zhu, B. Wei, *Chem. Soc. Rev.* **2016**, *45*, 3145.
- [11] A. Kinkhabwala, Z. Yu, S. Fan, Y. Avlasevich, K. Müllen, W. E. Moerner, *Nat. Photonics* **2009**, *3*, 654.
- [12] M. Wang, W. Li, L. Scarabelli, B. B. Rajeeva, M. Terrones, L. M. Liz-Marzan, D. Akinwande, Y. Zheng, *Nanoscale* **2017**, *9*, 13947.
- [13] J. Sun, H. Hu, D. Zheng, D. Zhang, Q. Deng, S. Zhang, H. Xu, *ACS Nano* **2018**, *12*, 10393.
- [14] D. Nepal, L. F. Drummy, S. Biswas, K. Park, R. A. Vaia, *ACS Nano* **2013**, *7*, 9064.
- [15] S. Y. Choi, C. T. Yip, G. C. Li, D. Y. Lei, K. H. Fung, S. F. Yu, J. Hao, *AIP Adv.* **2015**, *5*, 067148.
- [16] G. C. Li, Q. Zhang, S. A. Maier, D. Lei, *Nanophotonics* **2018**, *7*, 1865.
- [17] X. Qi, T. W. Lo, D. Liu, L. Feng, Y. Chen, Y. Wu, H. Ren, G. C. Guo, D. Lei, X. Ren, *Nanophotonics* **2020**, *9*, 2097.
- [18] Y. Zhang, W. Chen, T. Fu, J. Sun, D. Zhang, Y. Li, S. Zhang, H. Xu, *Nano Lett.* **2019**, *19*, 6284.
- [19] G. M. Akselrod, T. Ming, C. Argyropoulos, T. B. Hoang, Y. Lin, X. Ling, D. R. Smith, J. Kong, M. H. Mikkelsen, *Nano Lett.* **2015**, *15*, 3578.
- [20] J. Shi, J. Zhu, X. Wu, B. Zheng, J. Chen, X. Sui, S. Zhang, J. Shi, W. Du, Y. Zhong, Q. Wang, Q. Zhang, A. Pan, X. Liu, *Adv. Opt. Mater.* **2020**, *8*, 2001147.
- [21] J. Chen, Q. Zhang, J. Shi, S. Zhang, W. Du, Y. Mi, Q. Shang, P. Liu, X. Sui, X. Wu, R. Wang, B. Peng, H. Zhong, G. Xing, X. Qiu, T. C. Sum, X. Liu, *Commun. Phys.* **2019**, *2*, 80.
- [22] X. Zhang, S. Choi, D. Wang, C. H. Naylor, A. T. C. Johnson, E. Cubukcu, *Nano Lett.* **2017**, *17*, 6715.
- [23] J. T. Hugall, A. Singh, N. F. van Hulst, *ACS Photonics* **2018**, *5*, 43.
- [24] T. B. Hoang, G. M. Akselrod, M. H. Mikkelsen, *Nano Lett.* **2016**, *16*, 270.
- [25] R. Chikkaraddy, X. Zheng, F. Benz, L. J. Brooks, B. de Nijs, C. Carnegie, M. E. Kleemann, J. Mertens, R. W. Bowman, G. A. E. Vandenbosch, V. V. Moshchalkov, J. J. Baumberg, *ACS Photonics* **2017**, *4*, 469.
- [26] T. Ding, D. Sigle, L. Zhang, J. Mertens, B. de Nijs, J. Baumberg, *ACS Nano* **2015**, *9*, 6110.
- [27] B. C. Marin, S. W. Hsu, L. Chen, A. Lo, D. W. Zwissler, Z. Liu, A. R. Tao, *ACS Photonics* **2016**, *3*, 526.
- [28] M. Celebrano, X. Wu, M. Baselli, S. Grossmann, P. Biagioni, A. Locatelli, C. De Angelis, G. Cerullo, R. Osellame, B. Hecht, L. Duo, F. Ciccacci, M. Finazzi, *Nat. Nanotechnol.* **2015**, *10*, 412.
- [29] G. Grinblat, Y. Li, M. P. Nielsen, R. F. Oulton, S. A. Maier, *ACS Photonics* **2017**, *4*, 2144.
- [30] G. M. Akselrod, C. Argyropoulos, T. B. Hoang, C. Ciraci, C. Fang, J. Huang, D. R. Smith, M. H. Mikkelsen, *Nat. Photonics* **2014**, *8*, 835.
- [31] T. B. Hoang, G. M. Akselrod, C. Argyropoulos, J. Huang, D. R. Smith, M. H. Mikkelsen, *Nat. Commun.* **2015**, *6*, 7788.
- [32] C. Lumdee, B. Yun, P. G. Kik, *ACS Photonics* **2014**, *1*, 1224.
- [33] Y. Meng, Q. Zhang, D. Lei, Y. Li, S. Li, Z. Liu, W. Xie, C. W. Leung, *Laser Photonics Rev.* **2020**, *14*, 2000068.
- [34] G. C. Li, Y. L. Zhang, J. Jiang, Y. Luo, D. Y. Lei, *ACS Nano* **2017**, *11*, 3067.
- [35] P. Tonndorf, R. Schmidt, P. Bottger, X. Zhang, J. Borner, A. Liebig, M. Albrecht, C. Kloc, O. Gordan, D. R. Zahn, S. Michaelis de Vasconcellos, R. Bratschitsch, *Opt. Express* **2013**, *21*, 4908.
- [36] H. Sugimoto, S. Yashima, M. Fujii, *ACS Photonics* **2018**, *5*, 3421.
- [37] J. B. Lassiter, F. McGuire, J. J. Mock, C. Ciraci, R. T. Hill, B. J. Wiley, A. Chilkoti, D. R. Smith, *Nano Lett.* **2013**, *13*, 5866.
- [38] A. Lovera, B. Gallinet, P. Nordlander, O. J. F. Martin, *ACS Nano* **2013**, *7*, 4527.
- [39] F. Xiao, W. Zhu, W. Shang, T. Mei, M. Premaratne, J. Zhao, *Opt. Express* **2015**, *23*, 3236.
- [40] X. Wu, S. K. Gray, M. Pelton, *Opt. Express* **2010**, *18*, 23633.
- [41] H. P. Hughes, A. R. Beal, *J. Phys. C: Solid State Phys.* **1979**, *12*, 881.
- [42] C. Ciraci, A. Rose, C. Argyropoulos, D. R. Smith, *J. Opt. Soc. Am. B* **2014**, *31*, 2601.
- [43] J. A. Schuller, S. Karaveli, T. Schiros, K. He, S. Yang, I. Kyriassis, J. Shan, R. Zia, *Nat. Nanotechnol.* **2013**, *8*, 271.
- [44] P. Tonndorf, R. Schmidt, R. Schneider, J. Kern, M. Buscema, G. A. Steele, A. Castellanos-Gomez, H. S. J. van der Zant, S. Michaelis de Vasconcellos, R. Bratschitsch, *Optica* **2015**, *2*, 347.
- [45] D. Pommier, R. Bretel, L. E. P. Lopez, F. Fabre, A. Mayne, E. Boer-Duchemin, G. Dujardin, G. Schull, S. Berciaud, E. L. E. Moal, *Phys. Rev. Lett.* **2019**, *123*, 027402.
- [46] P. B. Johnson, R. W. Christy, *Phys. Rev. B* **1972**, *6*, 4370.
- [47] M. Amani, P. Taheri, R. Addou, G. H. Ahn, D. Kiriya, D. H. Lien, J. W. Ager, 3rd, R. M. Wallace, A. Javey, *Nano Lett.* **2016**, *16*, 2786.